ADVANCED FUNCTIONAL MATERIALS
www.afm-journal.de

Time-Dependent T_1–T_2 Switchable Magnetic Resonance Imaging Realized by c(RGDyK) Modified Ultrasmall Fe_3O_4 Nanoprobes

Chen Bai, Zhengyang Jia, Lina Song, Wei Zhang, Yi Chen, Fengchao Zang, Ming Ma, Ning Gu, and Yu Zhang**

To achieve the accurate diagnosis of tumor with the magnetic resonance imaging (MRI), nanomaterials-based contrast agents are developed rapidly. Here, a tumor targeting nanoprobe of c(RGDyK) modified ultrasmall sized iron oxide is reported with high saturation magnetization and high T_1-weighted imaging capability, attributed to a large number of paramagnetic centers on the surface of nanoprobes and rapid water proton exchange rate (inner sphere model), as well as strong superparamagnetism (outer sphere model). These nanoprobes could actively target and gradually accumulate at the tumor site with a time-dependent T_1–T_2 contrast enhancement imaging effect. In in vivo MRI experiments, the nanoprobes exhibit the best T_1 contrast enhancement at 30 min after intravenous administration, followed by gradually vanishing and generating T_2 contrast enhancement with increasing time at tumor site. This is likely due to time-dependent nanoprobes aggregation in tumor, in good agreement with in vitro experiment where aggregated nanoprobes display larger r_2/r_1 value (19.1) than that of the dispersed nanoprobes (2.8). This dynamic property is completely different from other T_1-T_2 dual-modal nanoprobes which commonly exhibit the T_1- and T_2-weighted enhancement effect at the same time. To sum up, these c(RGDyK) modified ultrasmall Fe_3O_4 nanoprobes have significant potential to improve the diagnostic accuracy and sensitivity in MRI.

1. Introduction

The magnetic resonance imaging (MRI) has been considered as the most powerful and indispensable medical diagnostic technology due to the noninvasive, nonionized, and radiation-free features.[1] Meanwhile, this method provides excellent submillimeter spatial resolution in anatomical and functional 2D/3D imaging, especially in soft tissue and organs. However, in clinical used, the low detection sensitivity of MRI may be the limitation of the subtle and accurate diagnosis.[2] To improve this point, some appropriate exogenous contrast agents, which could enhance the contrast between pathological lesions and surrounding tissues, were applied before MRI examination. The MRI contrast agents are mainly divided into two types, including positive enhancement (T_1-weighted) and negative enhancement (T_2-weighted) contrast agent.[3] Generally, two principal relaxation process, called longitudinal (or spin–lattice) and transverse (or spin–spin) relaxation, are represented in MRI, and the positive and negative contrast agents respectively shorten the longitudinal and transverse relaxation time which accelerate the relaxation process and enhance imaging contrast. Therefore, the definition of T_1, T_2, and r_1, r_2 is corresponding to relaxation times and relaxicities respectively in these processes.[4] The positive contrast agents are commonly designed by some paramagnetic materials, such as gadolinium and manganese complexes, which change energy loss of proton and provide bright signal in T_1-weighted imaging. Similarly, some superparamagnetic materials, like iron oxide

C. Bai, Z. Jia, Y. Chen, Dr. M. Ma, Prof. N. Gu, Prof. Y. Zhang
State Key Laboratory of Bioelectronics
Jiangsu Key Laboratory for Biomaterials and Devices
School of Biological Science and Medical Engineering and Collaborative Innovation Center of Suzhou Nano Science and Technology
Southeast University
Nanjing 210096, P. R. China
E-mail: guning@seu.edu.cn; zhangyu@seu.edu.cn
Dr. L. Song
Department of Radiology
Affiliated Hospital of Nanjing University of Chinese Medicine
Nanjing 210029, P. R. China
Dr. W. Zhang
The Jiangsu Province Research Institute for Clinical Medicine
The First Affiliated Hospital with Nanjing Medical University
Nanjing 210029, P. R. China
Dr. F. Zang
Jiangsu Key Laboratory of Molecular and Functional Imaging
Medical School
Southeast University
Nanjing 210009, P. R. China

DOI: 10.1002/adfm.201802281

nanoparticles, are often acted as negative contrast agents, which influence the loss of phase coherence and provide dark signal in T_2-weighted imaging.[5] In addition, the desirable T_1 contrast agents should have large r_1 and small r_2/r_1 ratio, and the favorable T_2 contrast agents should show the much huger r_2 value than r_1.[6]

To improve the contrast enhancement effect, different clinical-used contrast agents have been developed. There are two main elements, including Gd and Fe, chosen for clinical MRI contrast agents. Gadolinium (Gd) chelate (e.g., Gd-diethylene triamine pentaacetic acid) are extensively used as clinical T_1-weighted contrast agents due to the strong paramagnetism of Gd^{3+} which produced a decrease in spin–lattice relaxation time, causing brighter T_1 images.[7] However, there is still some potential risks of Gd-based positive contrast such as nephrotoxicity, which leads to nephrogenic systemic fibrosis in patients, especially who suffered from impaired kidney function.[8] In recent reports, gadolinium accumulation and deposition in the brain and body was also considered as the potential risk for the patients.[9] In terms of low toxicity, magnetic iron oxide nanoparticles would be the most promising contrast agents as the iron element naturally exists in human body.[10] Comparing with Gd chelate, iron oxide nanoparticles are mostly used as T_2-weigted contrast agents which produces a decrease in the spin–spin relaxation time and cause dark T_2 images. Since 1996, when Feridex has been approved as the contrast agents used for liver and spleen MRI, a large number of preclinical researches using iron oxide nanoparticles as MRI contrast agents have been performed.[11] For instance, preoperative staging of pancreatic cancer with MRI using iron oxide nanoparticles contrast agent was carried out in phase-IV clinical trial.

Even though iron oxide nanoparticles were predominately used as T_2-weighted contrast agents, multifarious nanomaterial design has been conducted to combine T_1- and T_2-weighted enhancement effects of these nanoparticles. Iron oxide nanoprobes with T_1–T_2 dual-modal magnetic resonance imaging ability were constructed by two main methods. The one is to design complex nanoprobes with iron oxide and other T_1-weighted elements. For example, a europium-doped iron oxide nanoparticle was facilely synthesized as T_1-T_2 contrast agent, and the relaxivity of it is obviously superior to the Fe_3O_4 or Eu_2O_3 nanoparticle.[12] In addition, a novel core/shell Fe_3O_4/Gd_2O_3 nanocube was designed as T_1–T_2 dual-modal contrast agent and it has the higher relaxivity of r_1 value of 45.24 mM^{-1} s^{-1} and r_2 value of 186.51 mM^{-1} s^{-1} under 1.5T measurement which was about double higher than Gd_2O_3 nanoparticle and Fe_3O_4 nanocube, respectively.[13] The other method is that iron oxide nanoparticles could inherently display T_1- and T_2- weighted imaging abilities with appropriate sizes and magnetizations. Demir and co-workers demonstrated that iron oxide nanoparticles with 9.7 nm size could serve as both T_1 and T_2 contrast agents. In addition, to acquire T_1-dominated contrast efficiency, the size of iron oxide should be further downregulated.[14] Hyeon and co-workers synthesized uniform and extremely small-sized (3 nm) iron oxide nanoparticles as efficient T_1 contrast agents with a high r_1 relaxivity of 4.78 mM^{-1} s^{-1} and low r_2/r_1 ratio. The probable mechanism is mainly attributed to the large number of paramagnetic centers on the nanoparticle surface due to the enhanced surface-to-volume ratio.[15]

The above dual-modal T_1–T_2 contrast abilities were acquired by simply change the T_1 or T_2 sequence with the same nanoprobes and the slice scanning of both modalities could be set at the same position.[16] These guaranteed the sensitivity magnitude of contrast probes at approximate level and realized the self-confirmed cross-validation of diagnostic accuracy. However, these nanoprobes commonly exhibit the T_1- and T_2-weighted contrast enhancement effects at the same time. Only few studies reported the nanoprobes with switchable T_1–T_2 dual-modal MRI abilities. Hyeon and co-workers synthesized pH-sensitive magnetic nanogranades, which changed T_2-weighted to T_1-weighted contrast effects by pH-induced variation from aggregates to dispersive nanoparticles.[17] Another example is that Mao and co-workers used sub-5 nm ultrafine iron oxide nanoparticles self-assembled in the acidic tumor interstitial environment to realize the T_1-weighted contrast switched to T_2-weighted contrast effect.[18] As these nanoprobes were accumulated at tumor site without active targeting, the switching time was long to 24 h. In our previous works, we synthesized the c(RGDyK) modified ultrasmall Fe_3O_4 nanoprobes and the application of these nanoprobes for T_1-weighted imaging of tiny hepatic tumors in vivo was verified.[19] Here, we further explain the possible T_1 and T_2 contrast enhancement mechanism of these nanoprobes and report that these nanoprobes could also act as time-dependent switchable T_1–T_2 MRI contrast agent. With the small core size (5 nm) and high r_1 value of 7.83 mM^{-1} s^{-1}, these nanoprobes exhibited excellent T_1 contrast effect. Due to the appropriate hydrodynamic size, they can gradually accumulate inside tumor interstitial space, leading to time-dependent transformation from T_1-weighted contrast effect (dispersive nanoparticles) to T_2-weighted contrast effect (aggregated nanopaticles). Furthermore, these nanoprobes modified by c(RGDyK) could efficiently target to integrin $\alpha_v\beta_3$ overexpressed endothelium cells on angiogenic tumor vessels, which accelerated the speed and the amount of accumulated nanoprobes at tumor site and shorten the transfer time of dual-modal contrast imaging.

2. Results and Discussion

2.1. Preparation and Characterizations of Fe_3O_4 Nanoparticles

Magnetic iron oxide (Fe_3O_4) nanoparticles are conventionally synthesized by aqueous or nonaqueous routes. Although the Fe_3O_4 nanoparticles generated by aqueous route are easily accessible, the size distribution of them is broad and crystallinity is undesirable.[20] To improve the monodispersity and crystallinity, the high-temperature thermal decomposition as a powerful nonaqueous route was chosen to synthesize Fe_3O_4 nanoparticles with strong superparamagnetism and MRI contrast enhancement ability.[18] The ultrasmall superparamagnetic Fe_3O_4 nanoparticles (USPIO), in this research, were prepared by thermal decomposition of $Fe(acac)_3$ as precursors in the presence of oleylamine and benzyl ether. The uniform and monodispersed hydrophobic USPIO shown in Figure S1 in the Supporting Information had relatively narrow size distribution with the core size of 5.4 nm. The

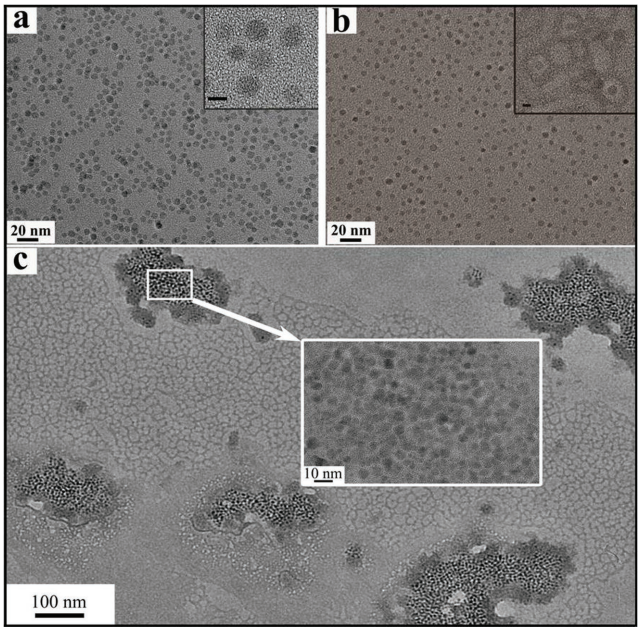

Figure 1. TEM images of a) RGD@USPIO (inset: HRTEM image. Scale bar, 5 nm), b) DSPE-PEG@USPIO (inset: with the phosphotungstic acid staining. Scale bar: 5 nm) and c) cross-linked RGD@USPIO.

selected-area electron diffraction and x-ray diffraction (XRD) results indicate an inverse spinel structure of iron oxide (Figure S2, Supporting Information).[21] As demonstrated in the previous work, the biocompatible carboxylated polyethylene glycol (PEG) was an effective ligand for transforming as-synthesized hydrophobic nanoparticles into aqueous medium. These PEGylated nanoparticles (PEG@USPIO) showed favorable biocompatibility.[19] In addition, the c(RGDyK) molecules was modified on the surface of PEG@USPIO to construct tumor-targeted nanoprobes (RGD@USPIO), and the main function of them had been evaluated through in vitro and in vivo studies, including targeting specificity and strong ability to resist against nonspecific uptake.[19] According to the transmission electron microscopy (TEM) and high-resolution TEM (HRTEM) images (**Figure 1**a), RGD@USPIO was in quasispherical shape with core size of 5 nm and high crystallinity. The hydrodynamic size of RGD@USPIO is about 13 nm which is larger than the TEM size, due to the surface PEG modification and thick hydration shell. This can provide strong steric hindrance effect against the nanoparticle aggregation. The saturated magnetic moment of RGD@USPIO was 50 emu g^{-1} Fe element mass, and the r_1 value of RGD@USPIO is 7.83 mM^{-1} s^{-1} (**Figure 2**b). This high saturation magnetization and r_1 value can provide powerful support to T_1-weighted contrast capability.

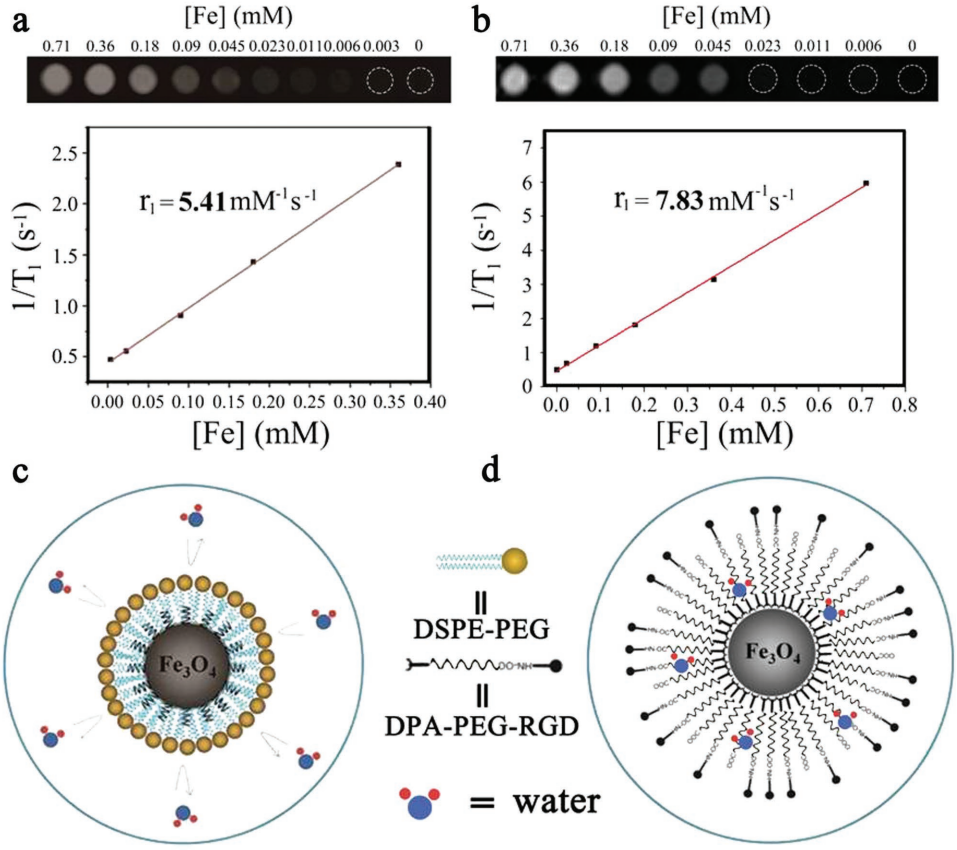

Figure 2. T_1-weighted MR images and $1/T_1$ against Fe concentration of a) DSPE-PEG@USPIO and b) RGD@USPIO. The values of r_1 were calculated from slopes of the corresponding linear fits of the experimental data. The schematic diagram of the interaction between the water proton and iron ion on the surface of c)DSPE-PEG@USPIO or (d)RGD@USPIO.

2.2. The T_1 Contrast Mechanism of Ultrasmall Fe_3O_4 Nanoprobes

From a molecular level viewpoint, the relaxation properties of clinical used paramagnetic materials are mainly related to the dynamic behaviors of water protons surrounding the nanoparticles. The inner sphere and outer sphere models are commonly used to explain the T_1 and T_2 contrast enhancement. Generally, T_1 relaxation is related to the inner sphere regime of paramagnetic centers where chemical exchange of proton occurs, and T_2 relaxation is attributed to the outer sphere regime where the proton's effective diffusion and interaction with the magnetic dipolar moment is dominant.[22] From the previous reports, the T_1 contrast mechanism of USPIO is commonly defined as the inner sphere models. As the unpaired electrons of the iron ion appeared on the surface, the water protons could effectively interact with these electrons. This interaction could increase the r_1 value of nanoparticles, which means the strong T_1-weighted contrast effects.[23] However, we deduced that the contribution from outer sphere regime at RGD@USPIO is also important for the strong superparamagnetic property of nanoparticles. To verify this hypothesis, the PEG-phospholipids (1, 2-distearoyl-*sn*-glycero-3-phosphoethanolamine-*N*-[methoxy (polyethylene glycol copolymers, distearoyl phosphoethanolamine (DSPE)-PEG2000) coated USPIO (DSPE-PEG@USPIO) were synthesized. The shape and crystalline of DSPE-PEG@USPIO is similar to RGD@USPIO (Figure 1b). The difference between these two nanoparticles was that there exists hydrophobic lipid bilayer on the surface of DSPE-PEG@USPIO, which effectively prevents the chemical exchange between the surface paramagnetic centers and water proton, and thus inhibits the contribution from the inner sphere regime. The r_1 value of DSPE-PEG@USPIO is about 5.41 mM^{-1} s^{-1} (Figure 2a). Even though the r_1 value decreased compared with that of RGD@USPIO (7.83 mM^{-1} s^{-1}), DSPE-PEG@USPIO still exhibited strong T_1 contrast effect. This result could effectively demonstrate that the outer sphere model is also main contribution to the T_1 relation of RGD@USPIO. Therefore, except the interaction between protons and nanoparticles affected the T_1 contrast enhancement of these nanoprobes, the effective interaction with the magnetic dipolar moment also attributed to this enhancement (Figure 2c,d).

2.3. In Vivo T_1-Weighed Imaging Using PEG@USPIO and RGD@USPIO Nanoprobes

The biosafety and targeting effect of PEG@USPIO and RGD@USPIO in vitro had been verified at the previous work.[19] To testify the stronger targeting ability of RGD@USPIO in vivo, the T_1 contrast enhancement effects of these two nanoprobes were compared (**Figure 3**a,b). Similarly, when injecting with these two nanoprobes, the T_1-weighted contrast MRI obviously enhanced. After injecting with RGD@USPIO, the tumor-to-tissue signal-to-noise ratio (SNR) calculated from MRI signal was increased rapidly and reached the maximum value which was 2.85 times stronger than preinjection. Besides electron spin resonance (ESR) effect, the stronger contrast enhancement of RGD@USPIO is also attributed to that c(RGDyK) molecules modified on the surface of nanoprobes can specifically recognize tumor angiogenesis and actively target to tumor tissue, which effectively elevated the accumulation of nanoprobes.[24] By comparison, the T_1 contrast enhancement with passive targeting PEG@USPIO injection was obviously weaker. After imaging test, the tumor tissue was collected and treated by the Prussian blue and immunohistochemical staining (Figure 3c,d). It could be observed that blue spots of RGD@USPIO nanoprobes localized on the integrin $\alpha_v\beta_3$ expressing tumor angiogenesis with CD31 brown color stained. However, the PEG@USPIO nanoprobes sporadically localized at the interval tumor tissue. This phenomenon supports that c(RGDyK) modification could efficiently target to integrin $\alpha_v\beta_3$ overexpressed endothelium cells on angiogenic tumor vessels, which accelerated accumulation of nanoprobes at tumor site. Furthermore, the pathological research of the tumor tissue and normal organs after RGD@USPIO injection at different time points was performed. As shown in Figure S3 in the Supporting Information, blue staining can be observed obviously in tumor tissue and the accumulation amount of nanoprobes were increased with increasing time. While only slightly amount of nanoprobes were observed at liver and spleen, and there were no nanoprobe accumulation at other normal organs. This excellent active targeting capability could be attributed to the ultrasmall size as well as PEG and c(RGDyK) modification.

2.4. Time-Dependent Switchable T_1–T_2-Weighed MRI In Vivo

Even though the RGD@USPIO nanoprobes showed the active targeting ability and provided the desirable T_1 contrast enhancement performance, the signal of MRI at tumor tissue was decreased gradually after 30 min postinjection (Figure 3b). This reduced signal was much more apparent with RGD@USPIO nanoprobes than PEG@USPIO. This phenomenon can be explained by that the time-dependent accumulation and aggregation of nanoprobes in tumor tissue can decrease the T_1 contrast enhancement effect.[25] From **Figure 4**a,b, although the signal of T_2-weighted MRI has no significant difference during 60–240 min, the T_2*-weighted MRI showed the gradually decreasing SNR value. This phenomenon was attributed to the different imaging meaning for T_2- and T_2*-weighted MRI sequences. In general, magnetic nanoparticles exhibit superb ability in shortening transverse relaxation times T_2 and T_2*.[26] The difference between these T_2- and T_2*-weighted imaging sequences is that spin-echo-based T_2-weighted imaging provides great anatomic details, while T_2*-weighted images generates more hypointense contrast when iron depositions appearance.[27] This means that T_2*-weighted MRI is more sensitive to magnetic nanoparticles. Therefore, as shown in Figure 4b, T_2*-weighted MRI signal exhibits sensitive variation to magnetic nanoprobe aggregation. The directed evidence of this process was obtained with biological TEM observation (Figure 4c,d). After 30 min postinjection, the nanoprobes were monodispersed and sporadic localized around tumor cells. By contrast, after 240 min postinjection, a large amount of nanoprobes accumulated at tumor tissue and generated apparent aggregation (Figure 4e).

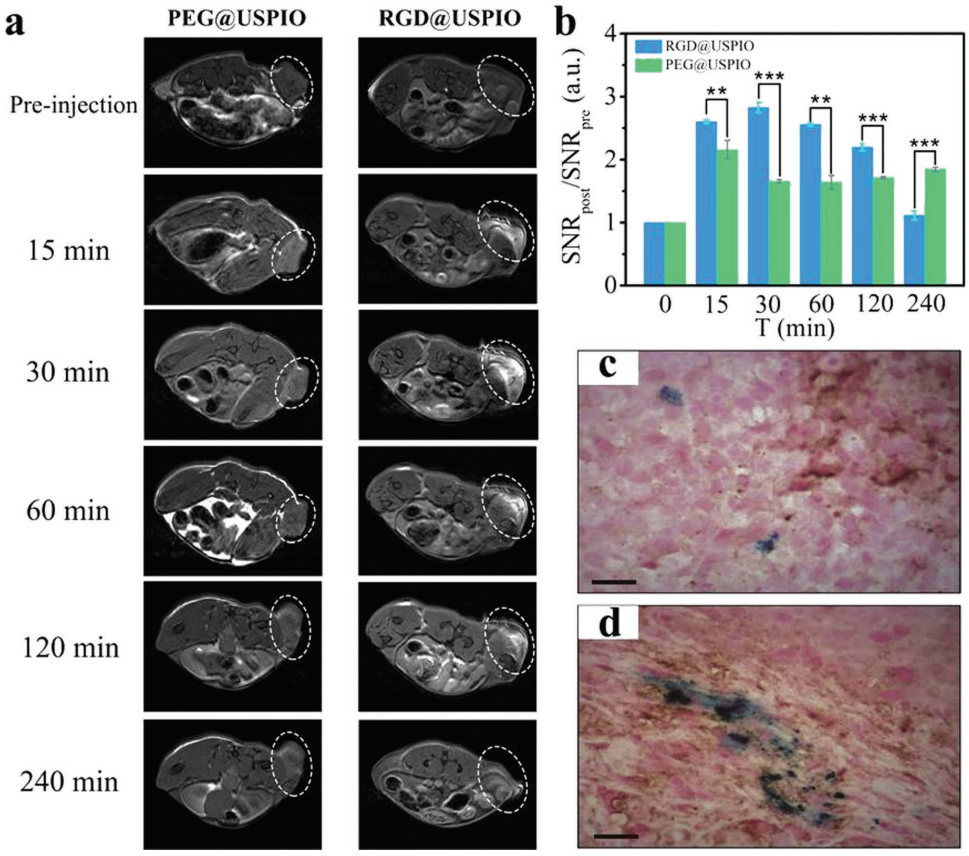

Figure 3. a) T_1-weighted MR images of tumor-bearing mice (white dashed circles) before and at the time points of 15, 30, 60, 120, and 240 min after the administration of RGD@USPIO and PEG@USPIO. b) Quantification of T_1 signal changes at the corresponding time points. The error bars represented ±s.d. of three independent experiments (**, $p < 0.01$; ***, $p < 0.001$). The histochemical and immunohistochemistry staining image of c) PEG@USPIO and d) RGD@USPIO 240 min postinjection (Scale bar: 20 μm).

In general, the principal effect of iron oxide nanoparticles with small core size is on T_1 relaxation in MRI and enhancement on T_2 relaxation effect can be obtained with the larger particle size.[28] Additionally, the relaxation is significantly affected by aggregation of magnetic nanoparticles.[29] Throughout the aggregation process, r_1 and r_2 relaxivity is decreased and increased respectively because the aggregated nanoparticles can be regarded as large magnetized spheres according to Langevin's law.[30] Thus, the probable mechanism of T_1–T_2 contrast effect in this article is mainly attributed to that time-dependent nanoprobe accumulation induced themselves to generate aggregation. This time-dependent aggregation mainly relies on the amount of accumulated nanoprobes with active targeting abilities in tumor tissue. Although the nanoprobes with small size can easily extravagate through tumor vessels and subsequently penetrate deeper into the tumor by EPR effect, the decrease of T_1 signal with PEG@USPIO in our research is not obvious from 60 to 240 min. However, with RGD@USPIO, this signal significantly decreased which potentially means the active targeting effect induced the time-dependent aggregation of nanoprobes at tumor site (Figure 3b). In this research, we used c(RGDyK) peptide modified nanoprobes which can effectively target angiogenic vessels and induce internalization via receptor-mediated endocytosis on endothelial cell at tumor site.[31] Several researches have been reported that c(RGDyK) modification can improve better iron oxide nanoparticles uptake and distribution. Sun and co-workers reported that ultrasmall c(RGDyK)-MC-Fe_3O_4 NPs were stable in physiological conditions and confirmed that the accumulation of c(RGDyK)-MC-Fe_3O_4 NPs at tumor was mediated by integrin $\alpha_v\beta_3$ binding.[32] Kiessling's group also demonstrated that a high density of RGD modified USPIO nanoprobes could be accumulated in the target cell to induce a significant signal change in MRI where receptor-mediated-specific uptake contributes to the accumulation of RGD-USPIO in cells.[33] From this point of views, we deduced that time-dependent aggregated nanoprobes can change T_1-weighted contrast effect to T_2-weighted contrast effect with c(RGDyK) peptide targeting.

Compared with the previous report of T_1–T_2 switchable nanoprobes, these active targeted nanoprobes showed the better MRI ability and the shorter switching time. In addition, these T_1–T_2 dual-modal nanoprobes could effectively elevate the reliability and accuracy of diagnosis, and reflected the dynamic accumulated progress of nanoprobes in tumor tissue.

To further investigate the effect of ultrasmall nanoparticles aggregation on T_1- and T_2-weighted imaging, we also cross-linked RGD@USPIO nanoprobes by glutaraldehyde (16 wt%) to form nanoparticle aggregates and compared them with monodispersive nanoprobes. As shown in TEM image (Figure 1c), after cross-linking, the hydrodynamic size of

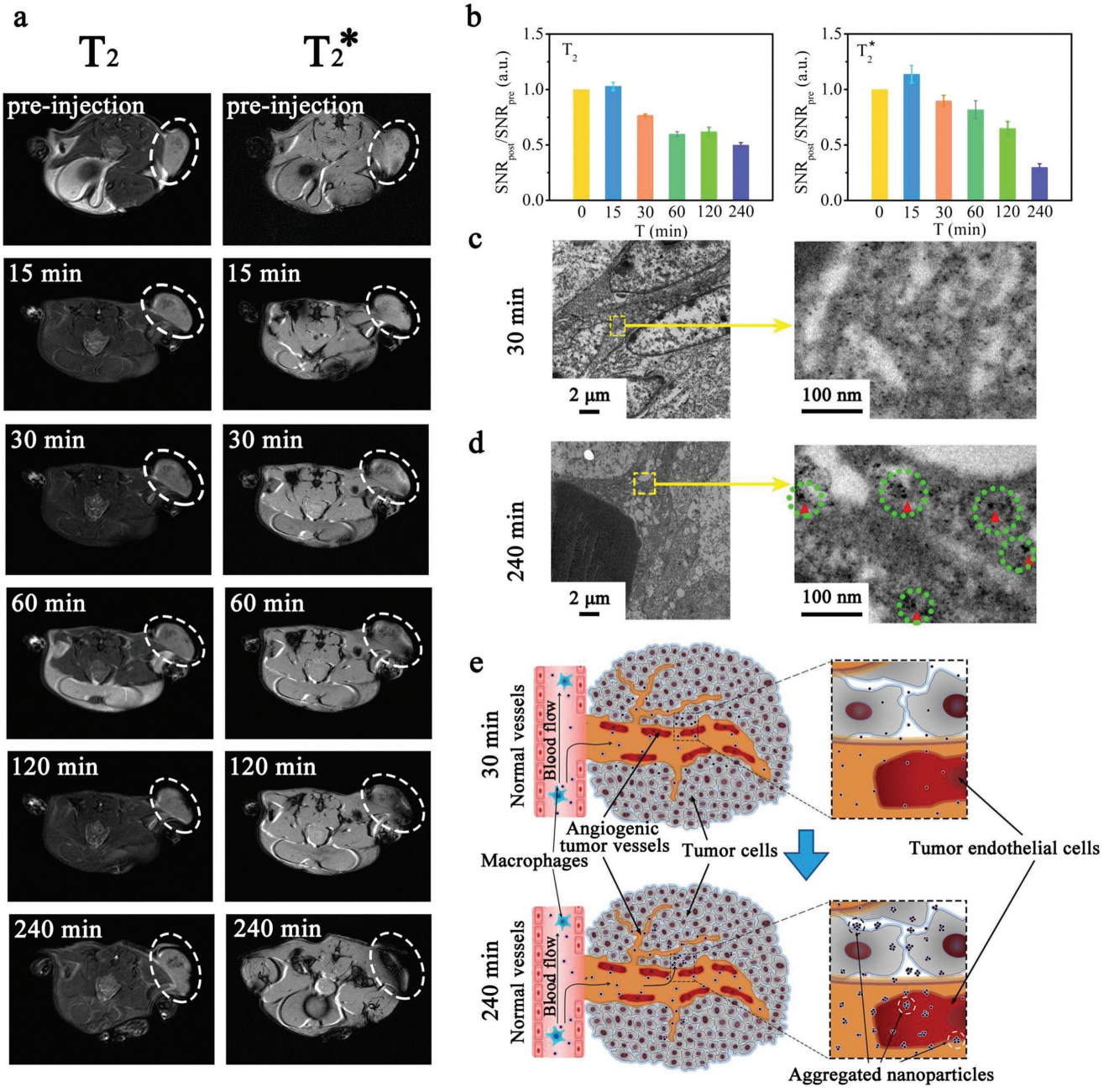

Figure 4. a)T_2-weighted and T_2*-weighted MR images of tumor-bearing mice (white dashed circles) before and at the time points of 15, 30, 60, 120, and 240 min after the administration of RGD@USPIO. b) Quantification of T_2 and T_2* signal changes at the corresponding time points. The error bars represented ± s.d. of three independent experiments. Biological TEM images of tumor tissue slices and the partial magnification showing the distribution of RGD@USPIO at c) 30 min and d) 240 min postinjection (the aggregated RGD@USPIO was indicated by red triangle and green circle). e)The schematic diagram of T_1-weighed contrast enhancement switched to T_2-weighted contrast enhancement with RGD@USPIO to actively target and accumulate in tumor leading to time-dependent transforming from dispersive to aggregated state.

RGD@USPIO was increased from 13 to 33 nm (**Figure 5**a), and the saturated magnetic moment was increased to 62 emu g^{-1} Fe element mass (Figure 5b). The increased saturated magnetic moment could be explained by Langevin's law. That is, comparing with the monodispersed nanoparticles, the aggregated nanoparticles could be considered as single nanoparticle with larger size, where magnetic dipolar interaction between nanoparticles in aggregated nanoparticles resulted in higher saturated magnetic moment than monodispersed nanoparticles.[30] The ESR measurement was also employed to confirm the aggregation effect.[34] The ΔH_{pp} of aggregated nanoparticle is 539G which is almost nonuple higher than monodispersed nanoparticles (Figure 5c). As indicated in previous report, the T_2 relaxation is the loss of phase coherence with the interaction of each spins.[35] Therefore, the stronger magnetic dipolar moment promotes the effect of T_2 contrast enhancement.

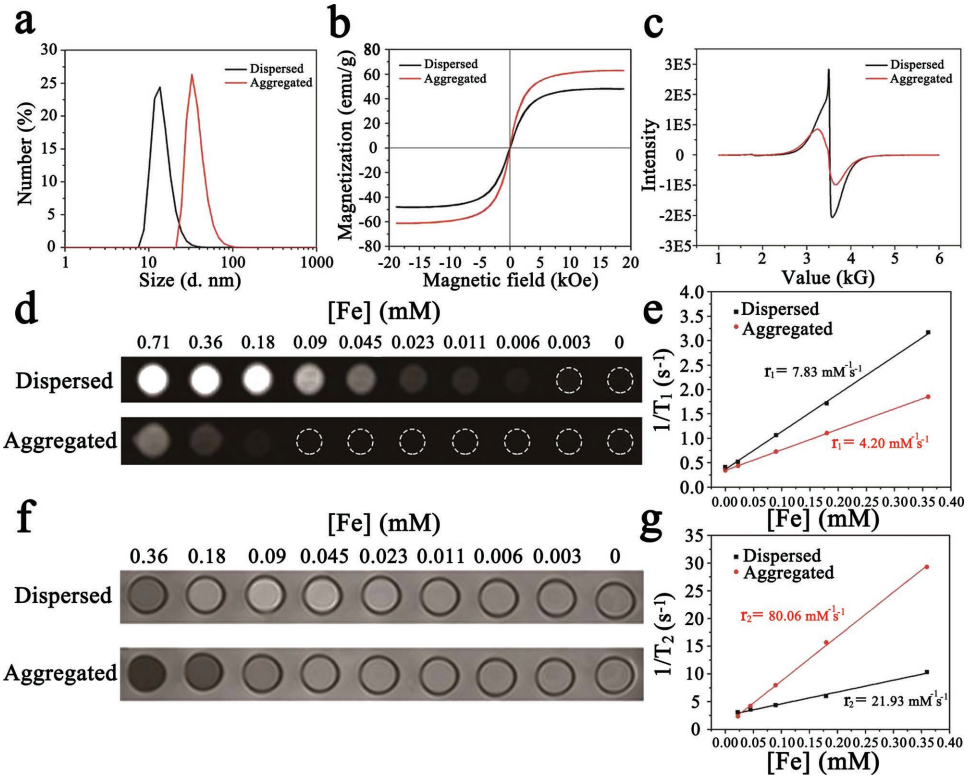

Figure 5. a) The hydrodynamic sizes of monodispersed and aggregated RGD@USPIO dissolved in water. b) Hysteresis loops and c) ESR spectrum of monodispersed and aggregated RGD@USPIO recorded at room temperture. d) T_1-weighted and f) T_2-weighted MR images and e) $1/T_1$ and g) $1/T_2$ against Fe concentration of monodispersed and aggregated RGD@USPIO.

As shown in Figure 5f,g, the r_2 value of aggregated nanoparticle was 80.06 mM^{-1} s^{-1}, which is much higher than monodispersed nanoparticles (21.93 mM^{-1} s^{-1}). In contrast, the T_1 contrast enhancement effect of aggregated nanoparticle was inhibited and the r_1 value was decreased to 4.20 mM^{-1} s^{-1} (Figure 5d,e). This is due to that nanoparticle aggregations reduces the specific surface area and thus decrease the chemical exchange between nanoparticle surface and water proton at inner sphere regime.[22b]

Due to the very fast crossing-linking velocity, the time-dependent aggregation process is difficult to be monitored by dynamic light scattering (DLS) and MRI measurements. So, we investigated the effect of aggregate size on T_1- and T_2-weighted imaging through adding different concentration of glutaraldehyde (0%–16%) and monitored their hydrodynamic size variation by DLS. As shown in Figure S4a,b in the Supporting Information, the hydrodynamic size increased with increasing concentration of glutaraldehyde. Meanwhile, the increased aggregation of nanoprobes resulted in the better T_2-weighted enhancement and the lower T_1-weighted enhancement (Figure S4c–f, Supporting Information). These could further demonstrate that with the aggregation of nanoprobes, the T_1-weighted enhancement can switch to T_2-weighted enhancement.

3. Conclusion

In summary, we demonstrated that c(RGDyK) modified ultrasmall Fe_3O_4 nanoprobes with the core size of 5 nm showed the favorable T_1-weighted contrast enhancement and the high r_1 value of 7.83 mM^{-1} s^{-1}. Different from the previous reports, the mechanism of the T_1 contrast enhancement was demonstrated not only by chemical exchange at inner sphere regime but also by the outer sphere model for strong superparamagnetism of ultrasmall nanoparticles. Furthermore, the time-dependent T_1–T_2 switchable contrast enhancement could be obtained in vivo, attributed to that actively targeting RGD@USPIO nanoprobes could easily accumulated in tumor, which accelerated the aggregation of nanoprobes and shortened the T_1 to T_2 transformation time. And this was further demonstrated by comparing aggregated nanoprobes with monodispersive nanoprobes in vitro.

4. Experimental Section

Materials: All materials were used as received without further purification. Iron(III) acetylacetonate ($Fe(acac)_3$, 98%), oleylamine (80%–90%), benzyl ether (97%), and hexane (98%) were obtained from Aladdin Industrial Co. 1-Ethyl-(3-3-dimethylaminopropyl) carbodiimide hydrochloride, *N*, *N*′-dicyclohexylcarbodiimide, *N*-hydroxysuccinimide and a,*ω*-*bis*{2-[(3-carboxy-1-oxopropyl)amino]ethyl}poly-(ethylene glycol) (carboxylated PEG, *M* = 2000) were obtained from Sigma-Aldrich. Dopamine hydrochloride was obtained from J&K Chemical. PEG-phospholipids (1, 2-distearoyl-*sn*-glycero-3-phosphoethanolamine-*N*-[methoxy (polyethylene glycol copolymers (DSPE-PEG2000) was purchased from Shanghai A.V.T. Pharmaceutical Ltd. c(RGDyK) peptide (*M* = 620) was purchased from GLS Biochem Ltd. Deionized water (DW) was purified by Millipore Water Purification System. 4T1 cell line was obtained from Institute of Biochemistry and Cell Biology (Shanghai, China) with recommended culture condition.

Preparation and Characterizations of Ultrasmall Iron Oxide Nanoprobes: The synthesis of ultrasmall superparamagnetic Fe_3O_4 nanoparticles(USPIO) and the PEGylated Fe_3O_4 nanoparticles(PEG@USPIO) and c(RGDyK) peptide modified nanoprobes (RGD@USPIO) were prepared as previously reported.[19] The DSPE-PEG2000-coated USPIO (DSPE-PEG@USPIO) was synthesized as previous method.[36] Briefly, 100 mg DSPE-PEG2000 and 5 mg USPIO were mixed and dissolved in 10 mL chloroform and 5 mL deionized water, then the chloroform was vaporized by evaporation (65 °C, 20 min) to obtain the water soluble DSPE-PEG@USPIO. The aggregated nanoprobes were prepared by glutaraldehyde cross-linking. Typically, different concentrations of glutaraldehyde including 2, 4, 8, and 16 wt% were added into the nanoprobe solution with the Fe concentration of 1 mg mL^{-1}, and DLS and MRI were measured subsequently. The morphology of the nanoparticles and selected-area electron diffraction pattern were carried on TEM and HRTEM imaging (JEOL, Japan). The XRD measurements were carried out on a powder sample of the USPIO (X'TRA, Switzerland). Hydrodynamic size of nanoparticles was measured by a dynamic light scattering (Malvern Zetasizer, UK) instrument. The iron concentration of Fe_3O_4 NPs was measured with a classical C-A (absorbance vs Fe concentration) calibration curve on a UV–vis spectrophotometer (UV-3600, Shimadzu, Japan). The magnetism of nanoparticles was carried out on vibrating sample magnetometer (VSM, Lakeshore 7407, USA) and electron spin resonance (ESR) spectrum (EMX-10/12.)

In Vitro MRI Studies: Magnetic nanoparticles were diluted into different concentrations for measuring the value of r_1 and r_2, and this measurement was carried out on a clinic 3.0T magnetic resonance (MR) scanner (Verio, Siemens, Germany) with a head coil. The absolute T_1 values of phantoms against different Fe contents were measured from the quantitative T_1 maps Modified Look-Locker Inversion Recovery sequence, and the parameters used for T_1-weighted imaging were as follows: flip angle = 35, TR = 284.38 ms, TE = 1.1 ms, TI = 88, 188, 2088, 2204, 4104, 4221, and 6121 ms, field of view (FOV) = 340 × 273, matrix = 144 × 224, slice thickness/gap = 5.0 mm/1.0 mm, and NEX = 8. The absolute T_2 values of phantoms from the quantitative T_2 maps were measured by the use of the True Fast Image with Steady-state Precession sequence with the following parameters: flip angle = 160, TR = 13200 ms, TE = 84, 176 and 268 ms, FOV = 334 × 334, matrix = 320 × 320, slice thickness/gap = 5.0 mm/1.0 mm and NEX = 1.

Animal Model: All animal experiments were conducted following a protocol approved by the Animal Care Committee of Southeast University. Female BALB/c mice with aged 6–8 weeks were purchased from the Model Animal Research Center of Southeast University. The experimental model of mice breast tumor was established by subcutaneous inoculation with 4T1 cells (1×10^6) injected into the right legs of mice. The tumors were allowed to grow 10–14 d with the tumor diameter of 5–10 mm for in vivo and ex vivo experiments.

In Vivo MRI Experiments: The PEG@USPIO or RGD@USPIO was intravenously injected into the mice with dose of 5 mg Fe kg^{-1}. T_1-weighted MR images across the tumor in transverse plane were carried out using Multi Slice Multi Echo method on a 7.0 T Micro-MR scanner (PharmaScan, Brukers, Germany). Parameters used for T_1-weighted imaging were as follows: flip angle = 180, TR = 498.3 ms, TE = 14.0 ms, FOV = 3 × 3, matrix = 256 × 256, SI = 1.0 mm/1.0 mm, averages = 3, slices = 16, NEX = 1. T_2-weighted MR images were acquired by rapid acquisition relaxation enhanced method with following parameters: flip angle = 180, TR = 2500.0 ms, TE = 33.0 ms, FOV = 3 × 3, matrix = 256 × 256, SI = 1.0 mm/1.0 mm, averages = 3, slices = 16, and NEX = 1. MR images were obtained before and at differential time points of 15, 30, 60, 120, and 240 min post administration. SNR was calculated for each mouse to qualify the signal enhancement in the region of interest (ROI) by the following equation: $SNR = SI/SD_{noise}$, where SI stands for signal intensity in ROIs and SD stands for standard deviation analyzed from the MR images. The values of SNR_{post}/SNR_{pre} were calculated to represent the signal changes.

Histochemical, Immunohistochemistry, and Biological TEM Analysis: For histochemical analysis, tumors and organs from experimental mice were excised and fixed in 10% neutral buffered formalin for 2 d. Then, the tissues were processed routinely into paraffin and sectioned into 5 mm, stained successively by Prussian blue for MNCs and nuclear fast red for the cell nucleus. Finally, the sections were rinsing with phosphate buffer saline and dehydrated by 70%, 80%, and 100% ethanol, then transferred into xylene, and mounted for optical microscopy examined. For immunohistochemical analysis, the tumor sections were first stained with primary rat antimouse CD31 antibody to show tumor angiogenesis. CD31 staining with brown color could be reached by using glucose oxidase-diaminobenzidine method. Then, Prussian blue and nuclear fast red staining procedures were virtually the same aforementioned and finally observed by optical microscopy. For biological TEM analysis, tumor tissues were fixed overnight with 2.5% glutaraldehyde and then cut into small pieces of ≈1 mm^3. Subsequently, the specimens were stained overnight using 1% uranyl acetate in the dark and were dehydrated using 25%–100% ethanol alcohol. Finally, these dehydrated specimens were embedded in resin, which was then cured in an oven at a temperature of 60 °C (2 d) for TEM observation.

Statistical Analysis: One-sample t-test statistical analysis was performed to evaluate the significance of the experimental data. A p value of 0.01 was selected as the level of significance. The data was indicated with (**) for $p < 0.01$ and (***) for $p < 0.001$.

Supporting Information

Supporting Information is available from the Wiley Online Library or from the author.

Acknowledgements

This research was supported by the National Key Research and Development Program of China (No. 2017YFA0205502), National Natural Science Foundation of China (No. 81571806, 81671820), The Science and Technology Support Project of Jiangsu Province (No. BE2017763), the Jiangsu Provincial Special Program of Medical Science (No. BL2013029), and the Fundamental Research Funds for the Central Universities.

Conflict of Interest

The authors declare no conflict of interest.

Keywords

magnetic resonance imaging, T_1-weighted imaging, T_2-weighted imaging, tumor, ultrasmall Fe_3O_4 nanoprobes

Received: April 2, 2018
Revised: May 14, 2018
Published online: June 22, 2018

[1] a) N. Lee, T. Hyeon, *Chem. Soc. Rev.* **2012**, *41*, 2575; b) H. Xing, S. Zhang, W. Bu, X. Zheng, L. Wang, Q. Xiao, D. Ni, J. Zhang, L. Zhou, W. Peng, K. Zhao, Y. Hua, J. Shi, *Adv. Mater.* **2014**, *26*, 3867; c) C. Tassa, S. Y. Shaw, R. Weissleder, *Acc. Chem. Res.* **2011**, *44*, 842.

[2] a) J. Gao, H. Gu, B. Xu, *Cheminform* **2009**, *42*, 1097; b) E. Terreno, D. D. Castelli, A. Viale, S. Aime, *Chem. Rev.* **2010**, *110*, 3019.

[3] a) M. Port, J. M. Ide, C. Medina, C. Robic, M. Sabatou, C. Corot, *BioMetals* **2008**, *21*, 469; b) T. Courant, V. Roullin, C. Cadiou,

M. Callewaert, M. C. Andry, C. Portefaix, C. Hoeffel, M. Goltstein, M. Port, S. Laurent, L. Elst, R. Muller, M. Molinari, F. Chuburu, *Angew. Chem., Int. Ed.* **2012**, *51*, 9119; c) Z. Zhou, D. Huang, J. Bao, Q. Chen, G. Liu, Z. Chen, X. Chen, J. Gao, *Adv. Mater.* **2012**, *24*, 6223.

[4] a) Z. Zhou, R. Bai, J. A. Munasinghe, Z. Shen, L. Nie, X. Chen, *ACS Nano* **2017**, *11*, 5227; b) N. Lee, D. Yoo, D. Ling, M. H. Cho, T. Hyeon, J. Cheon, *Chem. Rev.* **2015**, *115*, 10637.

[5] a) A. J. Villaraza, A. Bumb, M. W. Brechbiel, *Chem. Rev.* **2010**, *110*, 2921; b) L. Zhang, R. Liu, H. Peng, P. Li, Z. Xu, A. K. Whittaker, *Nanoscale* **2016**, *8*, 10491; c) A. Han, D. Choi, T. Kim, J. H. Lee, J. K. Kim, M. J. Yoon, K. S. Choi, S. W. Kim, *Chem. Commun.* **2009**, *44*, 6780; d) J. S. Choi, J. H. Lee, T. H. Shin, H. T. Song, E. Y. Kim, J. J. Cheon, *J. Am. Chem. Soc.* **2010**, *132*, 11015; e) H. Yang, Y. Zhuang, Y. Sun, A. Dai, X. Shi, D. Wu, F. Li, H. Hu, S. Yang, *Biomaterials* **2011**, *32*, 4584.

[6] Z. Li, P. W. Yi, Q. Sun, H. Lei, H. Zhao, Z. Zhu, S. Smith, M. Lan, G. Lu, *Adv. Funct. Mater.* **2012**, *22*, 2387.

[7] a) H. J. Weinmann, R. C. Brasch, W. R. Press, G. E. Wesbey, *Ajr Am. J. Roentgenol.* **1984**, *142*, 619; b) S. Aime, M. Botta, E. Terreno, *Adv. Inorg. Chem.* **2005**, *57*, 173

[8] P. H. Kuo, E. Kanal, A. K. Abu-Alfa, S. E. Cowper, *Radiology* **2007**, *242*, 647.

[9] V. M. Runge, *Invest. Radiol.* **2017**, *52*, 317.

[10] a) Y. W. Jun, J. H. Lee, J. Cheon, *Angew. Chem., Int. Ed.* **2008**, *47*, 5122; b) J. W. M. Bulte, D. L. Kraitchman, *NMR Biomed.* **2004**, *17*, 484; c) C. Corot, P. Robert, J. M. Idee, M. Port, *Adv. Drug Delivery Rev.* **2006**, *58*, 1471; d) M. Mahmoudi, H. Hosseinkhani, M. Hosseinkhani, S. Boutry, A. Simchi, W. S. Journeay, K. Subramani, S. Laurent, *Chem. Rev.* **2011**, *111*, 253.

[11] W. Volkmar, G.V. Diana, *Int. J. Nanomed.* **2015**, *10*, 1245.

[12] L. Yang, Z. Zhou, H. Liu, C. Wu, H. Zhang, G. Huang, H. Ai, J. Gao, *Nanoscale* **2015**, *7*, 6843.

[13] F. Li, D. Zhi, Y. Luo, J. Zhang, X. Nan, Y. Zhang, W. Zhou, B. Qiu, L. Wen, G. Liang, *Nanoscale* **2016**, *8*, 12826.

[14] V. K. Sharma, A. Alipour, Z. Soran-Erdem, Z. G. Aykuta, H. V. Demir, *Nanoscale* **2015**, *7*, 10519.

[15] B. Kim, N. Lee, H. Kim, K. An, Y. Park, Y. Choi, K. Shin, Y. Lee, S. Kwon, J. Park, T. Ahn, Y. Kim, W. Moon, S. Choi, T. Hyeon, *J. Am. Chem. Soc.* **2011**, *133*, 12624.

[16] J. S. Choi, J. H. Lee, T. H. Shin, H. T. Song, E. Y. Kim, J. Cheon, *J. Am. Chem. Soc.* **2010**, *132*, 11015

[17] D.S. Ling, W. Park, S.J. Park, Y. Lu, K. S. Kim, M. J. Hackett, B. H. Kim, H. Yim, Y. S. Jeon, K. Na, T. Hyeon, *J. Am. Chem. Soc.* **2014**, *136*, 5647.

[18] L. Wang, J. Huang, H. Chen, H. Wu, Y. Xu, Y. Li, H. Yi, Y. A. Wang, L. Yang, H. Mao, *ACS Nano* **2017**, *11*, 4582.

[19] Z. Jia, L. Song, F. Zang, J. Song, W. Zhang, C. Yan, J. Xie, Z. Ma, M. Ma, G. Teng, N. Gu, Y. Zhang, *Theranostics* **2016**, *6*, 1780.

[20] A. Szpak, G. Kania, T. Skorka, W. Tokarz, S. Zapotoczny, M. Nowakowska, *Nanopart Res.* **2013**, *15*, 1372.

[21] F. Hu, Q. Jia, Y. L, M. Gao, *Nanotechnology* **2011**, *22*, 245604

[22] a) S. Laurent, D. Forge, M. Port, A. Roch, C. Robic, L. Vander Elst, R. N. Muller, *Chem. Rev.* **2008**, *108*, 2064; b) Z. Zhou, Z. Zhao, H. Zhang, Z. Wang, X. Chen, R. Wang, Z. Chen, J. Gao, *ACS Nano* **2014**, *8*, 7976.

[23] a) L. R. Merte, G. Peng, R. Bechstein, *Science* **2012**, *336*, 889; b) J. Y. Park, M. J. Baek, E. S. Choi, *ACS Nano* **2009**, *3*, 3663; c) S. L. Pinho, S. Laurent, J. Rocha, *J. Phys. Chem. C.* **2012**, *116*, 2285.

[24] a) D. Hanahan, R. A. Weinberg, *Cell* **2011**, *144*, 646; b) P. Carmeliet, R. K. Jain, *Nature* **2000**, *407*, 249.

[25] Z. Zhou, L. Wang, X. Chi, J. Bao, L. Yang, W. Zhao, Z. Chen, X. Wan, X. Chen, J. Gao, *ACS Nano* **2013**, *7*, 3287.

[26] J. W. Bulte, T. Douglas, B. Witwer, S. C. Zhang, E. Strable, B. K. Lewis, H. Zywicke, B. Miller, P. van Gelderen, B. M. Moskowitz, I. D. Duncan, J. A. Frank, *Nat. Biotechnol.* **2001**, *19*, 1141.

[27] J. Huang, X. Zhong, L. Wang, L. Yang, H. Mao, *Theranostics* **2012**, *2*, 86

[28] a) Y. J. Wang, S. M. Hussain, G. P. Krestin, *Eur. Radiol.* **2001**, *11*, 2319; b) Y. J. Wang, *Quant. Imaging Med. Surg.* **2011**, *1*, 35; c) E. X. Wu, H. Tang, J. H. Jensen, *NMR Biomed.* **2004**, *17*, 478; d) U. I. Tromsdorf, O. T. Bruns, S. C. Salmen, U. Beisiegel, H. Weller, *Nano Lett.* **2009**, *9*, 4434.

[29] N. Lee, T. Hyeon, *Chem. Soc. Rev.* **2012**, *41*, 2575.

[30] P. Gillis, F. Moiny, R. Brooks, *Magn. Reson. Med.* **2002**, *47*, 257

[31] C. Zhang, M. Jugold, E. C. Woenne, T. Lammers, B. Morgenstern, M. M. Mueller, H. Zentgraf, M. Bock, M. Eisenhut, W. Semmler, F. Kiessling, *Cancer Res.* **2007**, *67*, 1555

[32] J. Xie, K. Chen, H. Y. Lee, C. Xu, A. R. Hsu, S. Peng, X. Chen, S. Sun, *J. Am. Chem. Soc* **2008**, *130*, 7542

[33] F. Kiessling, J. Huppert, C. Zhang, J. Jayapaul, S. Zwick, E. C. Woenne, M. M. Mueller, H. Zentgraf, M. Eisenhut, Y. Addadi, M. Neeman, W. Semmler, *Radiology* **2009**, *253*, 462.

[34] K. H. Wu, Y. C. Chang, H. B. Chen, *J. Magn. Magn. Mater.* **2004**, *278*, 156.

[35] C. Zhou, Q. Zhang, L. Chen, B. Han, G. Ni, J. Wu, D. Garg, H. Cheng, *J. Phys. Chem. C.* **2010**, *114*, 21405.

[36] J. Xie, C. Y. Yan, Y. Yan, L. Chen, L. N. Song, F. C. Zang, Y. L. An, G. J. Teng, N. Gu, Y. Zhang, *Nanoscale* **2016**, *14*, 16902.

